

American margin has been estimated at 1.7×10^9 mol/year by combining an estimate of the total SO_2 flux (2.1×10^{10} mol/year) with the median SO_2/N_2 ratio (12.6) derived from almost 100 analyses of volcanic gas chemistries in the region (39). The above flux can be corrected for air-derived N on the basis of measured N_2/Ar ratios and the assumption that Ar is derived from air. The revised value for the non-air N_2 flux from the Central American arc is 2.9×10^8 mol/year (39). This output flux balances almost exactly the input flux of N into the trench and implies that N is efficiently released from the slab and transported through the mantle wedge to the atmosphere by arc volcanism. Thus, the Central American subduction zone acts as a "barrier" (40) for the transport of sedimentary N into the mantle beyond the region of magma formation below the arc; that is, the N transfer from the crust to deep mantle is short-circuited by release through arc volcanism.

If the Central American subduction zone acts to efficiently recycle subducted sedimentary N to the atmosphere, the question arises whether subduction zones worldwide behave in an analogous fashion. The output of N from arcs globally has been estimated at 3.2×10^{10} mol/year, which corrects to a value of 2.0×10^{10} mol/year when the air-N contribution is subtracted (39). The input from subducted sediments is 1.37×10^{10} mol N/year, based on an estimate of the N concentration of 0.01 wt % (100 ppm) and a total flux of subducted sediment of 3.8×10^{15} g/year (39). Given the anticipated heterogeneity in N contents of various sediment lithologies (35) as well as the fact that sediments subducted worldwide are characterized by large compositional differences (41), we consider that the apparent difference between input and output estimates falls within the level of overall uncertainty. In this case, therefore, it would seem that sediments worldwide transport N to depths of arc magma generation only, and that recycling of subducted N to the surface via arc volcanism is extremely efficient. The corollary of this conclusion is that if surficial N is recycled into the deeper mantle [see (12)], then it would require a source (e.g., oceanic crustal basement) other than shallow marine sediments.

References and Notes

1. The $^{15}\text{N}/^{14}\text{N}$ ratio of a sample is reported in the delta notation where $\delta^{15}\text{N}_{\text{sample}} = \{[(^{15}\text{N}/^{14}\text{N})_{\text{sample}} / (^{15}\text{N}/^{14}\text{N})_{\text{AIR}}] - 1\} \times 1000$. The atmosphere (AIR) is the standard (= 0.0‰), so that $\delta^{15}\text{N}_{\text{sample}}$ represents the per mil deviation from this value.
2. M. Javoy, F. Pineau, H. Delorme, *Chem. Geol.* **57**, 41 (1986).
3. S. R. Boyd, C. T. Pillinger, *Chem. Geol.* **116**, 43 (1994).
4. P. Cartigny, S. R. Boyd, J. W. Harris, M. Javoy, *Terra Nova* **9**, 175 (1997).
5. P. Cartigny, J. W. Harris, M. Javoy, *Science* **280**, 1421 (1998).
6. B. Marty, F. Humbert, *Earth Planet. Sci. Lett.* **152**, 101 (1997).
7. B. Marty, L. Zimmermann, *Geochim. Cosmochim. Acta* **63**, 3619 (1999).
8. M. Javoy, *Geophys. Res. Lett.* **24**, 177 (1997).

9. N. Dauphas, F. Robert, B. Marty, *Meteorit. Planet. Sci.* **33**, A38 (1998).
10. I. N. Tolstikhin, B. Marty, *Chem. Geol.* **147**, 27 (1998).
11. M. Javoy, *Chem. Geol.* **147**, 11 (1998).
12. N. Dauphas, B. Marty, *Science* **286**, 2488 (1999).
13. K. E. Peters, *Limnol. Oceanogr.* **23**, 598 (1978).
14. M. Kienast, *Paleoceanography* **15**, 244 (2000).
15. R. Eppley, B. J. Peterson, *Nature* **282**, 677 (1979).
16. E. Wada et al., *Geochem. J.* **9**, 139 (1975).
17. J. D. Cline, I. R. Kaplan, *Mar. Chem.* **3**, 271 (1975).
18. M. J. Carr, *Volcanol. Geotherm. Res.* **20**, 231 (1984).
19. M. J. Carr, M. D. Feigenson, E. A. Bennett, *Contrib. Mineral. Petrol.* **105**, 369 (1990).
20. J. Aubouin et al., *Init. Rep. Deep Sea Dril. Proj.* **67**, 79 (1982).
21. R. B. Valentine, J. D. Morris, D. Duncan, *Eos* **78**, F673 (1997).
22. E. Moritz et al., *Earth Planet. Sci. Lett.* **174**, 301 (2000).
23. R. von Huene, C. R. Ranero, W. Weinrebe, K. Hinz, *Tectonics* **19**, 314 (2000).
24. T. Plank, C. H. Langmuir, *Nature* **362**, 739 (1993).
25. G. Kiruma et al., *Proc. Ocean Dril. Progr. Init. Rep.* **170**, 45 (1997).
26. L. C. Patino, M. J. Carr, M. D. Feigenson, *Contrib. Mineral. Petrol.* **138**, 265 (2000).
27. J. D. Morris, W. P. Leeman, F. Tera, *Nature* **344**, 31 (1990).
28. Materials and methods are available on Science Online.
29. Y. Sano, H. Wakita, *J. Geophys. Res.* **90**, 8729 (1985).
30. R. Poreda, H. Craig, *Nature* **338**, 473 (1989).
31. Other arc-related volcanoes analyzed for N systematics include Satsuma-Iwojima (42), Taupo Volcanic Zone (43), and Kudryavyy (44). Javoy et al. (2) showed that Poas has negative $\delta^{15}\text{N}$ values. A review of arc-related volcanic gases is provided by Giggenbach (45).
32. D. R. Hilton, K. Hammerschmidt, S. Teufel, H. Friedrichsen, *Earth Planet. Sci. Lett.* **120**, 265 (1993).
33. M. Gasparon, D. R. Hilton, R. Varne, *Earth Planet. Sci. Lett.* **126**, 15 (1994).
34. Hilton et al. (46) produced a "global" estimate of the isotopic composition of mantle wedge helium ($5.4 R_a$) based on a compilation of >1000 $^3\text{He}/^4\text{He}$ ratios at arcs worldwide.
35. Bebout (47) notes that the N concentration in oceanic pelagic sediments can vary from 70 to 600 ppm; however, pelagic limestone (100% calcite) may contain essentially no N.
36. G. Snyder, R. Poreda, A. Hunt, U. Fehn, *G-cubed* **2**, 2001G000163 (2001).
37. D. R. Hilton, A. M. Shaw, T. P. Fischer, *Eos* **82**, 1275 (2001).
38. A. M. Shaw, D. R. Hilton, T. P. Fischer, M. M. Zimmer, G. Alvarado, *Eos* **82**, 1303 (2001).
39. Hilton et al. (46) made N-input and N-output estimates for Central America and for arcs globally. In the case of Central America, the N-input estimate was based on a value of 7.7×10^{13} g sediment

- subducted over the entire length (1100 km) of the Central America trench (48).
40. Staudacher and Allègre (49) first used the term "barrier" in the context of processing noble gases at subduction zones.
41. Plank and Langmuir (48) calculate an average global subducting sediment (GLOSS) composition. The error on trace elements contents is 10 to 50%.
42. H. Shinohara, W. F. Giggenbach, K. Kazahaya, J. W. Hedenquist, *Geochem. J.* **27**, 271 (1993).
43. W. F. Giggenbach, *J. Volcanol. Geotherm. Res.* **68**, 89 (1995).
44. T. P. Fischer, W. F. Giggenbach, Y. Sano, S. N. Williams, *Earth Planet. Sci. Lett.* **160**, 81 (1998).
45. W. F. Giggenbach, in *Monitoring and Mitigation of Volcano Hazards*, R. Scarpa, R. Tilling, Eds. (Springer-Verlag, Berlin, 1996), pp. 221–256.
46. D. R. Hilton, T. P. Fischer, B. Marty, in *Noble Gases in Cosmochemistry and Geochemistry*, D. Porcelli, C. J. Ballentine, R. Wieler, Eds. (Mineralogical Society of America, Washington, DC, 2002), chapter 9.
47. G. E. Bebout, *Geophys. Monogr.* **98**, 179 (1996).
48. T. Plank, C. H. Langmuir, *Chem. Geol.* **145**, 325 (1998).
49. Th. Staudacher, C. J. Allègre, *Earth Planet. Sci. Lett.* **89**, 173 (1988).
50. M. Ozima, F. A. Podosek, *Noble Gas Geochemistry* (Cambridge Univ. Press, Cambridge, ed. 2, 2002).
51. Y. Sano, N. Takahata, Y. Nishio, T. P. Fischer, S. N. Williams, *Chem. Geol.* **171**, 263 (2001).
52. D. R. Hilton, *Chem. Geol.* **127**, 269 (1996).
53. A. M. Shaw et al., in preparation.
54. Air has $(\text{N}_2/\text{He})_A = 1.489 \times 10^5$ (50). $(\text{N}_2/\text{He})_M$ of the mantle is taken as 150 using a compilation of global N-MORB values (7). $(\text{N}_2/\text{He})_S = 10,500$ is obtained by combining an estimate of 2.1×10^4 for the crustal N_2/Ar ratio (57) with a $^4\text{He}/^{40}\text{Ar}$ production ratio of 2 (50).
55. See (52) for details of the correction procedure. Measured ratios are reported in (53).
56. $K = (\text{N}_2/\text{He})_{\text{sediment}} / (\text{N}_2/\text{He})_{\text{mantle}}$. Adopting end member compositions from (54) gives a K value of 70 (i.e., 10,500/150).
57. Supported by NSF grants EAR-0079402 MARGINS and EAR-0003668 (T.P.F.), EAR-0003628 (D.R.H.), and EAR-0003664 (J.A.W.). G. Alvarado and E. Molina provided logistical support during field work, and we thank C. Ramirez, B. Cameron, E. Mickelson, W. Suiter, and J. Hlebica for field assistance. V. Tudorei helped with N isotope analyses. We thank two anonymous reviewers for helpful comments.

Supporting Online Material

www.sciencemag.org/cgi/content/full/297/5584/1154/DC1
Materials and Methods

15 May 2002; accepted 10 July 2002

Splay Fault Branching Along the Nankai Subduction Zone

Jin-Oh Park,* Tetsuro Tsuru, Shuichi Kodaira, Phil R. Cummins, Yoshiyuki Kaneda

Seismic reflection profiles reveal steeply landward-dipping splay faults in the rupture area of the magnitude (*M*) 8.1 Tonankai earthquake in the Nankai subduction zone. These splay faults branch upward from the plate-boundary interface (that is, the subduction zone) at a depth of ~10 kilometers, ~50 to 55 kilometers landward of the trough axis, breaking through the upper crustal plate. Slip on the active splay fault may be an important mechanism that accommodates the elastic strain caused by relative plate motion.

Large thrust earthquakes along subduction zones pose a seismic and tsunami threat to densely populated coastal cities. These earth-

quakes can be generated repeatedly on a certain portion of the plate-boundary interface (*I*), which is called the seismogenic zone.

The seaward updip limit of the seismogenic zone helps to determine the size of the tsunami, whereas the landward downdip limit helps to determine the intensity of the strong ground motion, both of which may be generated by a large earthquake in the seismogenic zone. A thrust-type reverse-fault branching upward from the subduction zone at depth is often referred to as a “splay fault.” Fukao (2) pointed out the importance of such splay faults, which may provide a mechanism by which earthquakes generate tsunamis. Even though slip on splay faults has been inferred in various convergent margins related to large earthquakes from paleoseismology and crustal deformation modeling (2–8), there are few seismic reflection images of such faults to use in directly mapping the fault geometry. Among these subduction zones, the Nankai subduction zone (Fig. 1) off southwest Japan is known as one of the best-suited convergent plate margins for studying subduction zone earthquakes. Historically, large earthquakes along subduction zones have occurred with a recurrence interval of 100 to 200 years (9) along the Nankai Trough margin. The last two large earthquakes that occurred off the Kii Peninsula were the 1944 Tonankai ($M = 8.1$) and 1946 Nankaido ($M = 8.3$) events.

Multichannel seismic (MCS) reflection profiles (10) show splay faults in the rupture area of the 1944 Tonankai earthquake. The MCS profile on line 5 (Fig. 2A) reveals a unique, landward dipping, ~30-km-long thrust fault that branches upward from the plate-boundary interface at a depth of ~10 km, ~55 km landward from the deformation front (trough axis) in the forearc basin. This thrust fault becomes steeper (with an 8° to 20° dip) as it approaches the sea floor just seaward of the outer ridge, breaking through the upper crustal plate. Because the thrust fault almost reaches the sea floor and is apparently within the 1944 Tonankai coseismic rupture area estimated from tsunami (11) and seismic (12) waveform inversions, we suggest that it corresponds to a splay fault branching upward from the subduction zone plate boundary. This splay fault may have experienced slip during the 1944 Tonankai event. A splay fault with similar structural features was also identified on other MCS profiles on lines 4, 6, and 7 in the 1944 Tonankai coseismic rupture area, although a strong reflection from the splay fault was not observed at depths shallower than ~5 km. On line 4 (Fig. 2D), the fault branches upward from the plate-boundary interface at ~50 km landward from the trough axis. On line 7 (Fig. 2E), the splay fault with a steeper angle (with a 15° to 25° dip)

branches upward from the plate-boundary interface at a depth of ~10 km, ~55 km landward from the trough axis. The uppermost crustal sequence at the seaward tip of the forearc basin shows apparent landward-dipping bedding planes (Fig. 2, B and E), indicating substantial uplift of the outer ridge. Slip on the splay fault may heave the seaward tip of the forearc basin upward, producing a conspicuous sea-floor scarp and a subsequent outer ridge, which are in good agreement with geologic evidence (13). We observed several active normal faults (Fig. 2, B and D) cutting through

the uplifted crustal layers. These active normal faults may indicate an ongoing postseismic (or interseismic) relaxation after the coseismic slip on the splay fault, which would support the suggestion that the splay fault is closely related to the recent large event.

We note the reverse polarity reflection (Fig. 2C) of the splay fault, which may indicate elevated fluid pressure in the fault zone (14, 15). Recent submersible observations (16) were made of chemosynthetic benthic colonies around the sea-floor scarp of the splay faults, indicating the presence of cold seeps (Fig. 2A)

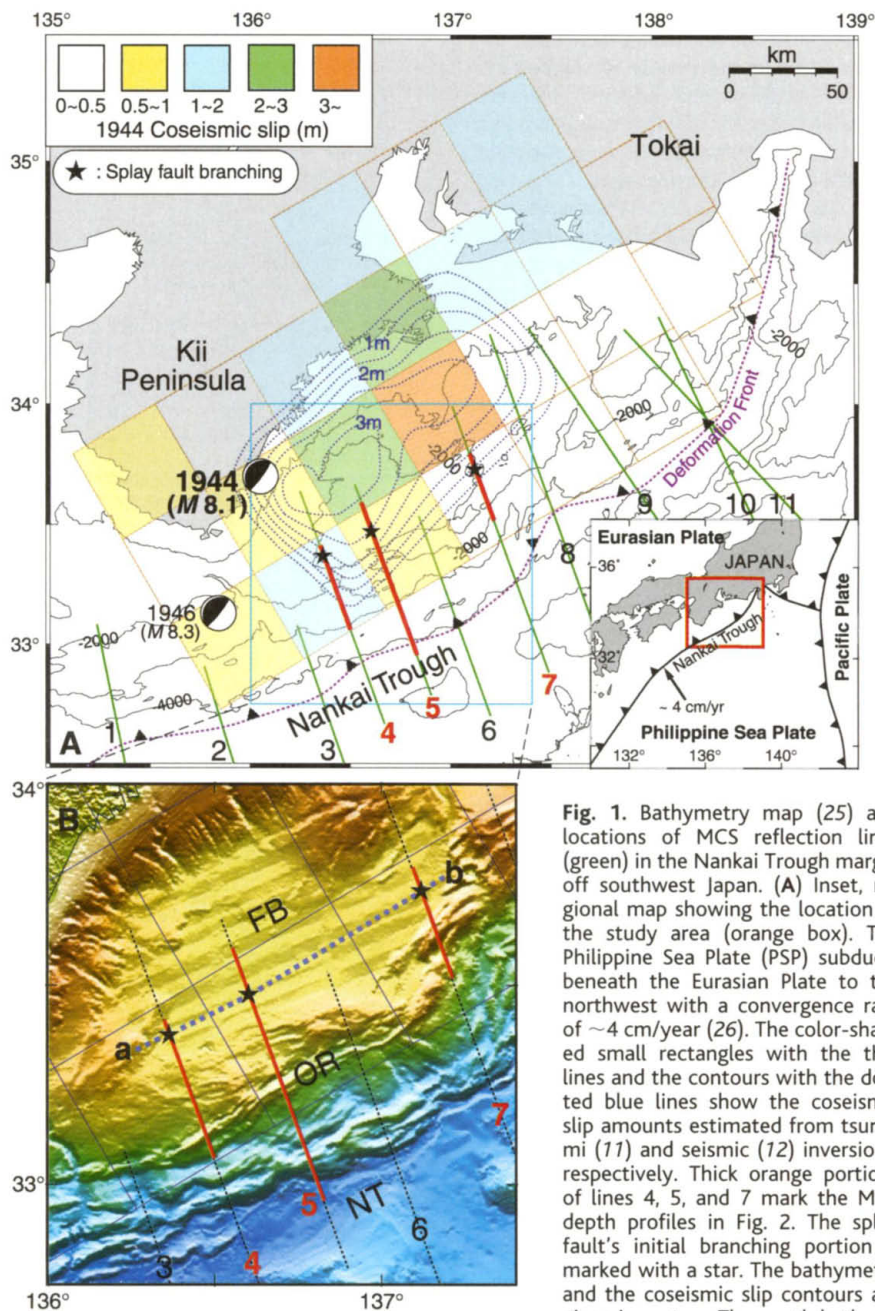


Fig. 1. Bathymetry map (25) and locations of MCS reflection lines (green) in the Nankai Trough margin off southwest Japan. (A) Inset, regional map showing the location of the study area (orange box). The Philippine Sea Plate (PSP) subducts beneath the Eurasian Plate to the northwest with a convergence rate of ~4 cm/year (26). The color-shaded small rectangles with the thin lines and the contours with the dotted blue lines show the coseismic slip amounts estimated from tsunami (11) and seismic (12) inversions, respectively. Thick orange portions of lines 4, 5, and 7 mark the MCS depth profiles in Fig. 2. The splay fault's initial branching portion is marked with a star. The bathymetry and the coseismic slip contours are given in meters. The swath bathymetry data are represented by the large rectangle with the light blue line, producing sea-floor relief topography (B). The Nankai Trough (NT), outer ridge (OR), and forearc basin (FB) are well defined in the topography. Most of the splay fault occurrence zone between the branching portion (line a to b) and the outer ridge is within the 1944 coseismic rupture area.

Institute for Frontier Research on Earth Evolution, Japan Marine Science and Technology Center, Yokosuka 237-0061, Japan.

*To whom correspondence should be addressed. E-mail: jopark@jamstec.go.jp

and possible fluid migration along the fault. Stick-slip behavior in a fault zone requires that the strength be recovered after any slip event so that the earthquake failure can repeat (17). Enhanced mineral precipitation caused by active fluid migration could contribute to the healing of the splay fault. As a weak fault zone, the splay fault is likely to be repeatedly chosen as

an easier pathway than the main subduction zone for rupture propagation of earthquakes. In particular, the 1944 Tonankai rupture area preserves the slip behavior on the splay fault as sea-floor topography. A combination of swath-bathymetric (Fig. 1) and MCS (Fig. 2, A, D, and E) data exhibit a pronounced, continuous outer ridge of topography longer than 120 km

along the strike, which we believe is caused by the splay fault slip in the 1944 Tonankai event. This outer ridge topography suggests repeating slip on the splay fault during the historic earthquake cycles, rather than the topography having been caused by an isolated event. Moreover, anomalously high gamma-ray intensity and U-series radioactive nuclide concentration (18) at

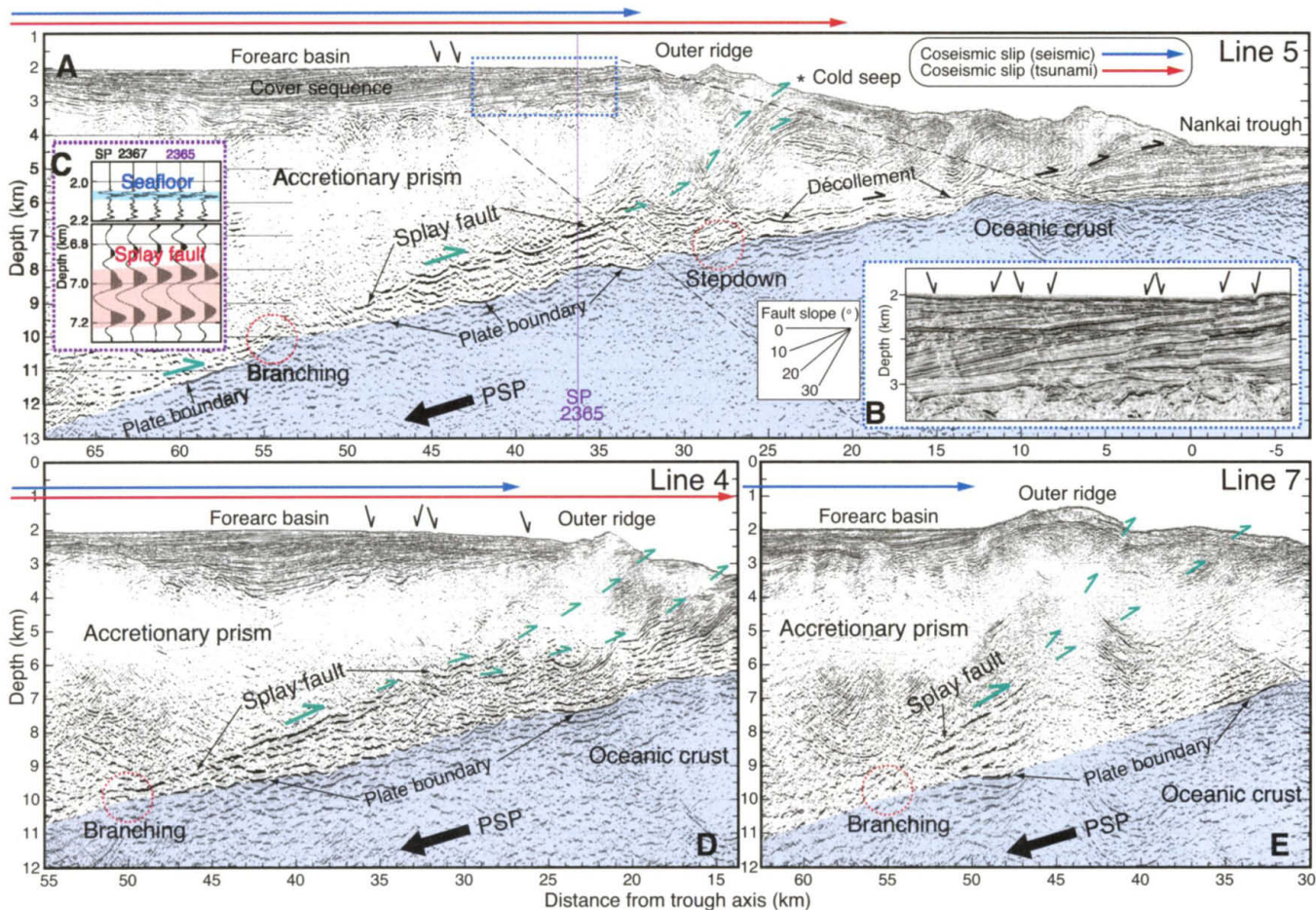


Fig. 2. Poststack depth-migrated MCS profiles showing the splay faults. The subducting oceanic crust is shaded light blue. The seaward distribution of the 1944 Tonankai coseismic slips estimated from tsunami (orange lines) and seismic (blue lines) inversions is projected in the profiles. Locations of both the splay fault's initial branching and the décollement stepdown to the top of the oceanic basement are marked in orange dotted circles. Green and black arrows show motions of the splay fault slip and the décollement or normal fault, respectively. Vertical

exaggeration is 2X. **(A)** MCS profile on line 5. The PSP subducting beneath the upper plate produces a huge accretionary prism. The location of the cold seep is marked by an asterisk. Note active normal faults **[(B), inset]** cutting the well-stratified, landward-tilting cover sequence and reverse polarity reflection **[(C), inset]** of the splay fault at a depth of ~7 km around the shot point (SP) 2365. **(D)** The active normal faults are also observed on line 4. **(E)** The splay fault is also identified on line 7, which is separated from line 4 by an ~80-km distance.

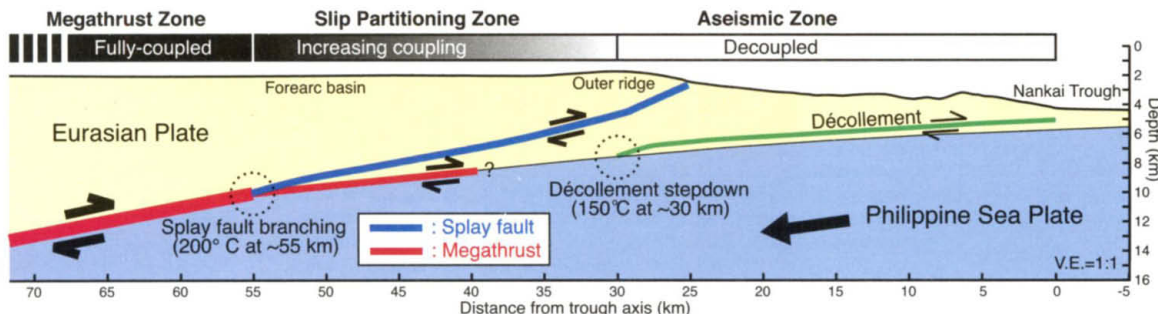


Fig. 3. Schematic cross section of the updip portion of the Nankai subduction zone. Gradation in gray scale shows the degree of interplate coupling. Temperature at the plate boundary is inferred from thermal modeling results (20).

the cold seep sites (Fig. 2A), which may be attributed to the formation of microcracks in the fracture zone of the active fault (19), support the hypothesis that the splay fault is one of the major active faults in the Nankai subduction zone. Slip on the active splay fault may be an important mechanism that accommodates elastic strain due to relative plate motion.

All of the interseismic elastic strain at the updip portion of the seismogenic zone could be released by the coseismic splay fault slip alone, but it seems more likely that there would be slip partitioning between it and the subduction zone (Fig. 3). The splay fault's initial branching portion (Figs. 1 and 2) is within the 1944 Tonankai coseismic rupture area, suggesting a causal relation between the earthquake and slip partitioning. Even though we cannot distinguish the splay fault slip from the subduction zone slip, the splay fault may be responsible for tsunami earthquake generation, accompanying deformation of the forearc accretionary wedge.

The updip limit of the seismogenic zone is constrained by the structural extent of the splay fault and the outer ridge topography, which we believe accumulated during repeated earthquake cycles. Namely, the splay fault's intersection portion with the megathrust (Fig. 3), to which the 1944 coseismic rupture propagated, can be regarded as the "true" updip limit of the seismogenic zone to generate large earthquakes along the subduction zone. Based on thermal modeling (20), the temperature at the true updip limit corresponds to $\sim 200^\circ\text{C}$, which is greater than the $\sim 150^\circ\text{C}$ threshold temperature proposed as the onset of stick-slip behavior (20). The $\sim 150^\circ\text{C}$ temperature corresponds to the temperature at a portion where the décollement steps down to the top of the oceanic crust under the outer ridge (Figs. 2A and 3).

Finally, structural features such as the décollement stepdown (150°C at ~ 30 km) and the splay fault branching (200°C at ~ 55 km) enable us to divide the updip portion of the Nankai subducting plate boundary into three different zones (Fig. 3): (i) a decoupled aseismic zone, (ii) a slip partitioning transition zone, and (iii) a coupled seismic zone. For the decoupled aseismic zone between the trough axis (0 km) and the outer ridge, ~ 30 km landward from the trough axis, the presence of stably sliding clays leads to free slip along the décollement (21). Underneath the outer ridge, the décollement steps down to the top of the oceanic crust (Fig. 2A) and the incipient plate-boundary coupling (locking) occurs because of dehydration of clay minerals (21), indicating the onset of interplate stick-slip and seismogenic behavior. The plate-boundary coupling may mature landward in the slip partitioning zone between the décollement stepdown portion and the splay fault branching portion, which can be treated as a transition zone from aseismic to seismic behavior. The splay fault is in the transition zone

and may partition some slip to the surface, where it can help generate a tsunami. The branching portion of the splay fault in the seismic zone is coupled to the subduction zone and may help generate large earthquakes along the plate boundary.

References and Notes

1. B. W. Tichelaar, L. J. Ruff, *J. Geophys. Res.* **98**, 2017 (1993).
2. Y. Fukao, *J. Geophys. Res.* **84**, 2303 (1979).
3. T. Kato, *Tectonophysics* **96**, 31 (1983).
4. J.-O. Park et al., *Geophys. Res. Lett.* **27**, 1033 (2000).
5. P. R. Cummins, T. Hori, Y. Kaneda, *Earth Planets Space* **53**, 243 (2001).
6. G. Plafker, *J. Geophys. Res.* **77**, 901 (1972).
7. S. H. Clarke, G. A. Carver, *Science* **255**, 188 (1992).
8. K. R. Berryman, Y. Ota, A. G. Hull, *Tectonophysics* **163**, 185 (1989).
9. M. Ando, *Tectonophysics* **27**, 119 (1975).
10. For deep-penetration seismic imaging, an air gun array with a large volume (~ 200 liters) was used as the controlled sound source. Velocity-depth models for the depth migration of reflection data were iteratively constructed by prestack depth migration-velocity analysis (22). Wide-angle data (23) guided the velocity analysis. The final velocity measurement for the depth migration has an $\sim 10\%$ maximum uncertainty at levels deeper than ~ 10 km.

11. Y. Tanioka, K. Satake, *Geophys. Res. Lett.* **28**, 1075 (2001).
12. M. Kikuchi, Y. Yamanaka, *Seismo* **7**, 6 (2001).
13. Y. Sugiyama, *Geofis. Int.* **33**, 53 (1994).
14. G. F. Moore, T. H. Shipley, *Proc. Ocean Drill. Program. Sci. Results* **131**, 73 (1993).
15. T. H. Shipley, G. F. Moore, N. L. Bangs, J. C. Moore, P. L. Stoffa, *Geology* **22**, 411 (1994).
16. J. Ashi, S. Kuramoto, S. Morita, U. Tsunogai, K. Kameo, *Eos* **82** (fall suppl.), T41A (2001).
17. J. C. Moore, D. Saffer, *Geology* **29**, 183 (2001).
18. M. Hattori, M. Okano, *JAMSTEC J. Deep Sea Res.* **20**, 37 (2002).
19. G. Igarashi et al., *Science* **269**, 60 (1995).
20. R. D. Hyndman, K. Wang, M. Yamano, *J. Geophys. Res.* **100**, 15373 (1995).
21. P. Vrolijk, *Geology* **18**, 703 (1990).
22. Z. Liu, N. Bleistein, *Geophysics* **60**, 142 (1995).
23. A. Nakanishi et al., *J. Geophys. Res.* **107**, EPM 2-1 (2002).
24. A. Asada, K. Okino, *Proc. Jpn. Soc. Mar. Surv. Technol.* **10**, 15 (1998).
25. Bathymetry data were compiled by the Hydrographic Department, Japan Maritime Safety Agency (24).
26. T. Seno, S. Stein, A. E. Gripp, *J. Geophys. Res.* **98**, 17941 (1993).
27. We thank the captain, crew, and technical staff of the R/V *Kairei*. Discussion with the Integrated Ocean Drilling Program Nankai Trough seismogenic zone research group was useful for completion of the initial manuscript.

17 May 2002; accepted 1 July 2002

Photothermal Imaging of Nanometer-Sized Metal Particles Among Scatterers

David Boyer,¹ Philippe Tamarat,¹ Abdelhamid Maali,¹ Brahim Lounis,^{1*}† Michel Orrit^{2*}

Ambient optical detection of labeled molecules is limited for fluorescent dyes by photobleaching and for semiconducting nanoparticles by "blinking" effects. Because nanometer-sized metal particles do not optically bleach, they may be useful optical labels if suitable detection signals can be found. We demonstrate far-field optical detection of gold colloids down to diameters of 2.5 nanometers with a photothermal method that combines high-frequency modulation and polarization interference contrast. The photothermal image is immune to the effects of scattering background, which limits particle imaging through Rayleigh scattering to diameters larger than 40 nanometers.

An ideal optical label for large molecules should generate an intense optical signal; it should also be small, durable, chemically inert, and apt to bind to the molecule of interest in a controlled manner. All present-day optical markers fall short of the "ideal label" status. The most common labels, fluorescent dyes, can be chemically grafted to the molecule under study. Their redshifted fluorescence can be sifted very efficiently out of the scattering background (1). Their

main drawback, however, is photobleaching, i.e., the irreversible photochemical processes leading from the excited fluorophore to nonfluorescent products. Nanocrystals of II-VI semiconductors (such as CdSe/ZnS) have recently been proposed as optical markers (2, 3). Although they resist bleaching longer than dyes, their luminescence brightness is liable to "blinking" (4), and they are difficult to functionalize in a controlled way.

Metal particles are currently used for single-particle or single-molecule tracking (5) and in immunocytochemistry (6, 7). They include colloids with diameters ranging from a micrometer to a few nanometers, and synthesized clusters (8, 9) with well-defined chemical structures. Submicrometer metal particles down to diameters of 40 nm can be imaged in an optical

¹Physique Moléculaire Optique et Hertzienne, CNRS et Université Bordeaux I, 351 Cours de la Libération, 33405 Talence Cedex, France. ²Huygens Laboratory, Universiteit Leiden, Postbus 9504, 2300 RA Leiden, Netherlands.

*These authors contributed equally to this work.
†To whom correspondence should be addressed. E-mail: lounis@cpmoh.u-bordeaux.fr